ACS OMEGA

http://pubs.acs.org/journal/acsodf

Article

Green and Facile Synthesis of Porous SiO_2@C Adsorbents from Rice Husk: Preparation, Characterization, and Their Application in Removal of Reactive Red 120 in Aqueous Solution

Tran Quoc Toan, Tran Kim Ngan, Do Tra Huong, Phuoc-Anh Le, Nguyen Thi Thuy,* Nguyen Nhat Huy, Dang Van Thanh, Nguyen Manh Khai, and Nguyen Thi Mai*

Cite This: *ACS Omega* 2023, 8, 9904−9918

Read Online

ACCESS | Metrics & More | Article Recommendations

ABSTRACT: In this work, a green, novel, fast, and facile approach for synthesizing a SiO_2/C nanocomposite series from rice husk (RH) through quenching and grinding techniques has been reported along with its application for the adsorptive removal of Reactive Red 120 (RR120) dye from an aqueous solution. The effect of carbonization temperature on the textural and interfacial features of RH was confirmed by scanning electron microscopy (SEM), while the structure and elemental composition of the as-synthesized RH were investigated via XRD, Brunauer−Emmett−Teller (BET), FT-IR, Raman, and X-ray photoelectron spectroscopy (XPS). The RH had a high surface area (521.35 m^2 g^{-1}), large micropores, mesopores, and total pore volumes of 0.5059, 3.9931, and 5.2196 cm^3 g^{-1}, while SiO_2 and C were the two major components. In the batch adsorption test, the effects of pH, contact time, adsorbent mass, temperature, and initial RR120 concentration were investigated. The maximum adsorption capacity was fitted by Langmuir, Freundlich, Temkin, Dubinin−Radushkevich (D−R), Hasley, Harkins−Jura, and BET isotherm models, and Langmuir was the best-fitted model. In addition, the pseudo-first-order, pseudo-second-order, intraparticle diffusion, and Elovich chemisorption models were used to explain the adsorption kinetics. Additionally, the values of Gibbs free energy, enthalpy, and entropy thermodynamics suggested that the RR120 adsorption phenomenon by RH8-3 was endothermic and spontaneous. The adsorption process was controlled by a physical mechanism, and the maximum adsorption capacity was found to be 151.52 mg g^{-1} at pH 2, with a contact time of 90 min, adsorbent amount of 0.03 g, and temperature of 313 K. The adopted technique may open up a new alternative route for the mass utilization of RH for the removal of dyes in water and wastewater and also for various practical applications.

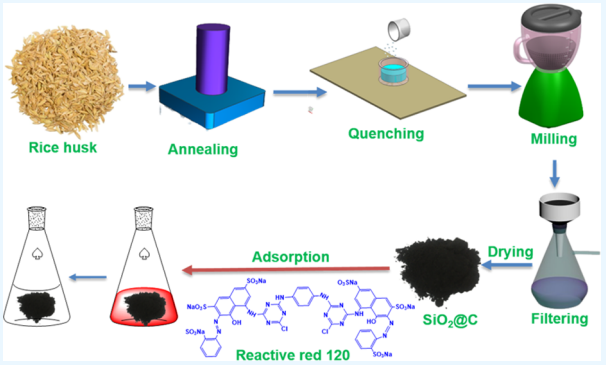

1. INTRODUCTION

Reactive Red 120 (RR120), a type of azo dye (approximately 9.9 million tons used per year)[1] with a complicated organic structure, has been extensively used in the textile industry[2] because the chemical, biological, and photocatalytic stability is very high. Due to these stable and durable properties, the degradation of RR120 by exposure to sunlight, detergents, water, and microorganisms is very difficult. The presence of RR120 in water is a cause for serious environmental pollution[3] because it can break down to form toxic amines and benzene, which can easily penetrate the water and cause anoxic conditions for plants and aquatic species. In addition, RR120 is also carcinogenic, mutagenic, and allergenic to exposed organisms. From the aspect of environmental safety, removing dyestuffs such as RR120 from wastewater is extremely necessary. Although a variety of methods have been applied for the dye removal, the adsorption technique is preferable due to its simplicity, simple unit assembly, high efficiency, and low cost.[4]

Rice husk is considered to be the main waste produced in a large amount (e.g., approximately 9 million tons in Vietnam) from the rice industry.[5,6] Burning is the first choice for the treatment of this waste because of its simplicity and the ability to produce energy. However, it not only emits polluted gas but also creates extremely fine silica ash, a toxic and hazardous constituent for health due to its long-time suspension in the air.[7] In addition, even a careful incineration process cannot completely convert rice husk to airborne silica. Thus, burning with releasing polluted smoke and fine ash has proven to be an

Received: November 1, 2022
Accepted: February 28, 2023
Published: March 7, 2023

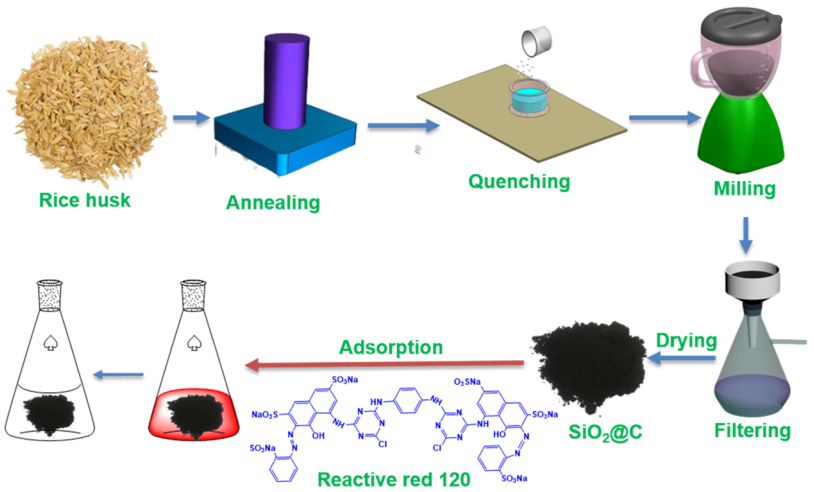

Figure 1. Process for the production of SiO_2/C nanoplates from rice husk (RHs) and their adsorption of RR120.

inappropriate solution. Fortunately, rice husk contains both essential C and Si; thus, it is beneficial for the fabrication of nanocomposites containing SiO_2 and C, which can be employed as a great anode material for lithium-ion batteries[8] or an effective adsorbent for the removal of pollutants in aqueous solutions.[9−20] Consequently, intensive efforts have been made in exploiting rice husk as a low-cost source for synthesizing SiO_2/C composites or carbon/Si-based materials. The methods include a sol−gel technique combined with mechanical milling,[21] steam activation,[22] hydrothermal coupling with a NaOH etching route,[9] calcination cooperating with a magnesiothermic reduction reaction,[7] calcination of the pyrolyzed rice husk in a NaOH solution,[22,23] and post-heat treatment processes before hydrolysis of tetraethyl orthosilicate to form SiO_2 shells on organic sphere templates followed by calcination in the air.[24] Actually, these as-mentioned methods have been successfully employed for synthesizing SiO_2/C nanocomposites[25] or carbon/Si-based materials. However, they require complicated equipment, high-cost and toxic precursors, template precursors, and multistep synthetic processes, which are not appropriate pathways for large-scale production. Therefore, it is desirable to find out a facile, cost-effective, and environmentally benign strategy to produce SiO_2/C nanocomposites.

Quenching is a process of heating followed by instant cooling to obtain the desired material properties.[26] It is most commonly used to harden steel by inducing a martensite transformation, where the steel must be rapidly cooled through its eutectoid point.[27] In addition, it is also used for reducing the crystal grain size of both metallic and plastic materials including increasing their hardness.[28] Although quenching is extensively applied to strengthen and harden steel and cast iron alloys in metallurgy and materials science,[29] there is still limited scientific literature on these aspects, especially for synthesizing SiO_2/C materials from waste rice husk.

In this work, we report a novel and facile approach for mass-producing SiO_2/C hybrids via the combustion-like rapid annealing and quenching of rice husk in water. The as-prepared SiO_2/C hybrid is composed of tiny SiO_2 particles implanted in porous carbon nanoplates or SiO_2 nanoparticles embedded in porous carbon nanoplates, which could be used for various applications. The advantages of this method are simple and fast synthesis, low cost, uncomplicated equipment, unreplenished chemicals, no toxic and dangerous wastes, and available mass production to obtain hybrid materials with the main components of SiO_2 and carbon. In addition, it could provide high surface area, large pore volume, and small average pore size, which are beneficial for the removal of organic compounds in aqueous matrices, especially organic dyes as well as applications for the energy field.

2. MATERIALS AND METHODS

2.1. Materials. The rice husk was collected at a rice milling factory located in Thai Nguyen Province (Vietnam) and washed with double-distilled water several times to eliminate dust and further dried in the air.

2.2. Experimental Process. The preparation of RH is illustrated in Figure 1. First, 10 g of rice husk was added to a graphite crucible with 5 mm thickness and then placed in a self-made vertical oven. The oven was programmed to reach 800 °C (RH8 series) or 900 °C (RH9) within different burning times as shown in Table 1. The black powder in the graphite crucible was quickly thrown into the water for rapid quenching and then collected by filtration. This material was then milled in a mixture of 200 mL of ethanol and double-distilled water solution with a ratio of 3:1 v/v using a Panasonic MX-900MW multitasking blender. After milling, the as-produced material was collected by filtration and dried at 80 °C for 24 h in a vacuum oven. After the pulverization process, the final product (denoted as RH_S) was sieved with a size of 0.1 mm and stored in a desiccator for characterization.

Table 1. Conditions for the Production of the RH Series

no.	sample name	burning time	burning temperature (°C)
1	RH8-1	2 h	800
2	RH8-2	8 h	800
3	RH8-3	5 min	800
4	RH9-1	5 min	900

2.3. Adsorption Experiments. The studies of Reactive Red 120 (RR120) adsorption were conducted in a batch method (Figure 1). The ζ-potential was recorded by following experiments from somewhere else.[30] In adsorption, the RR120 solutions at various concentrations (40−200 mg L^{-1}) were prepared and their initial pH solutions (1.0−10.0) were adjusted by adding 0.1 M HCl or NaOH solution. Typically, a certain amount of RH was transferred into 250 mL Erlenmeyer flasks containing 50 mL of aqueous solution. The mixture was then

https://doi.org/10.1021/acsomega.2c07034
ACS Omega 2023, 8, 9904−9918

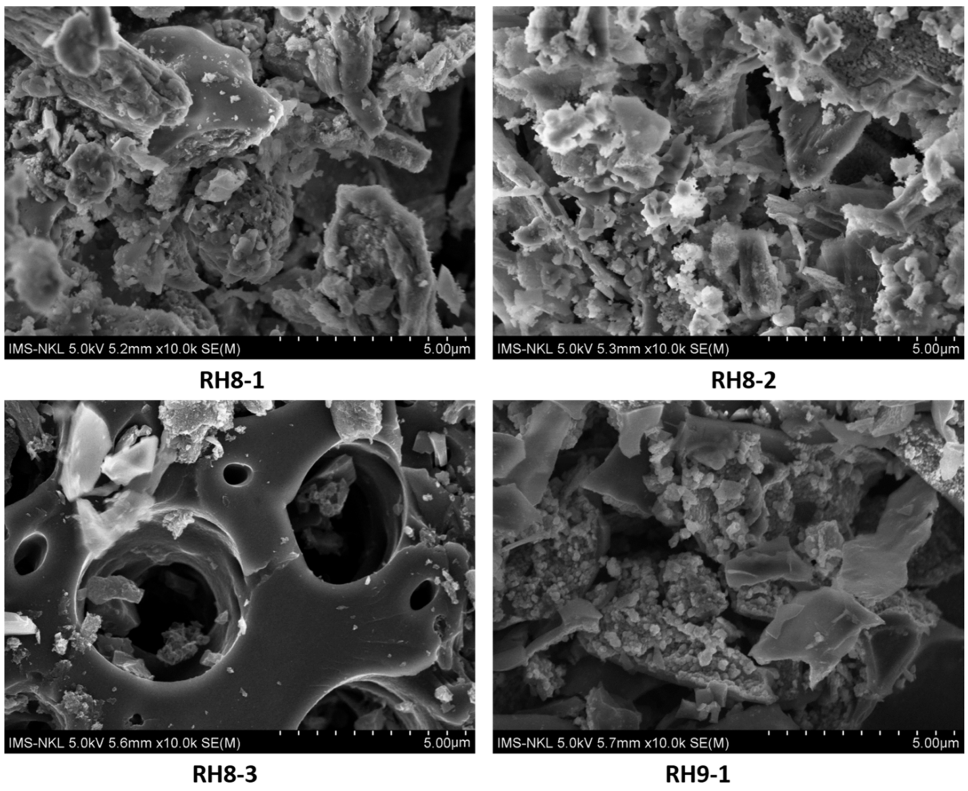

Figure 2. SEM images of RH8-1, RH8-2, RH8-3, and RH9-1.

shaken at 200 rpm for a certain time at a certain temperature. After reaching the equilibrium time, the mixture was centrifuged at 5000 rpm for 5 min to remove the solids. The supernatant liquid was collected for determining the absorbance using an ultraviolet−visible (UV−Vis) spectrophotometer (Hitachi UH5300) at a wavelength of 510 nm. The removal effectiveness (E%) and adsorbed amount of RR120 (q_e, mg L^{-1}) under equilibrium conditions were calculated by the following equation

$$E = \frac{C_o\text{-}C_e}{C_o} \times 100\% \quad (1)$$

$$q_e = \frac{C_o\text{-}C_e}{m} \times V \quad (2)$$

where C_o and C_e (mg L^{-1}) are the initial and equilibrium RR120 concentrations, respectively, m (g) is the mass of the adsorbent, and V (L) is the volume of the RR120 solution.

The extent of adsorption of RR120 from the aqueous solution relies on the initial RR120 concentration. The adsorption isotherms were studied with different RR120 concentrations (from 50 to 200 mg L^{-1}) at pH 2 using 0.03 g of the RH8-3 adsorbent, at 30 °C, for 3 h, at 200 rpm, and mixed with a 50 mL RR120 solution. The data were fitted and calculated in terms of the following isotherm models:

The Langmuir (eq 3), Freundlich (eq 4), Temkin (eq 5), D−R (eq 6), Halsey (eq 7), Harkins−Jura (eq 8), and Brunauer−Emmett−Teller (BET) (eq 9) models were applied to describe the adsorptive behavior of RR120 on the RH material.

$$\frac{C_e}{q_e} = \frac{1}{q_{max}K_L} + \frac{1}{q_{max}}C_e \quad (3)$$

$$\ln q_e = \ln K_F + \frac{1}{n}C_e \quad (4)$$

$$q_e = \left(\frac{RT}{b_T}\right)\ln a_T + \left(\frac{RT}{b_T}\right)\ln C_e \quad (5)$$

$$\ln q_e = K\varepsilon^2 + \ln q_{D-R} \quad (6)$$

$$\ln q_e = \frac{1}{n}\ln k - \frac{1}{n}\ln\left[\ln\left(\frac{1}{C_e}\right)\right] \quad (7)$$

$$\frac{1}{q_e^2} = \frac{B}{A} - \frac{1}{A}\ln C_e \quad (8)$$

$$\frac{C_e}{q_e(1 - C_e)} = \frac{1}{q_{max}k} + \frac{k-1}{q_{max}k}C_e \quad (9)$$

where q_e is the adsorption capacity of RR120 (mg g^{-1}), q_{max} is the maximum adsorption capacity, C_e is the equilibrium concentration, n, k, K, a, b, A, and B are constant parameters for the isotherm equations, q_{D-R} is the D−R maximum adsorption capacity of the RR120 (mg g^{-1}), and ε is the Polanyi potential given by the equation below

$$\varepsilon = RT\ln(1 + 1/C_e) \quad (10)$$

where R is the gas constant (R = 8.314 J K^{-1} mol^{-1}) and T is the temperature (K).

In addition, the adsorption kinetics of RR120 on RH was studied to explain the mechanism that participated in the adsorption of RR120 ions from the solution in various adsorption times. To do this, four kinetic models are used, including pseudo-first-order, pseudo-second-order, intraparticle

https://doi.org/10.1021/acsomega.2c07034
ACS Omega 2023, 8, 9904−9918

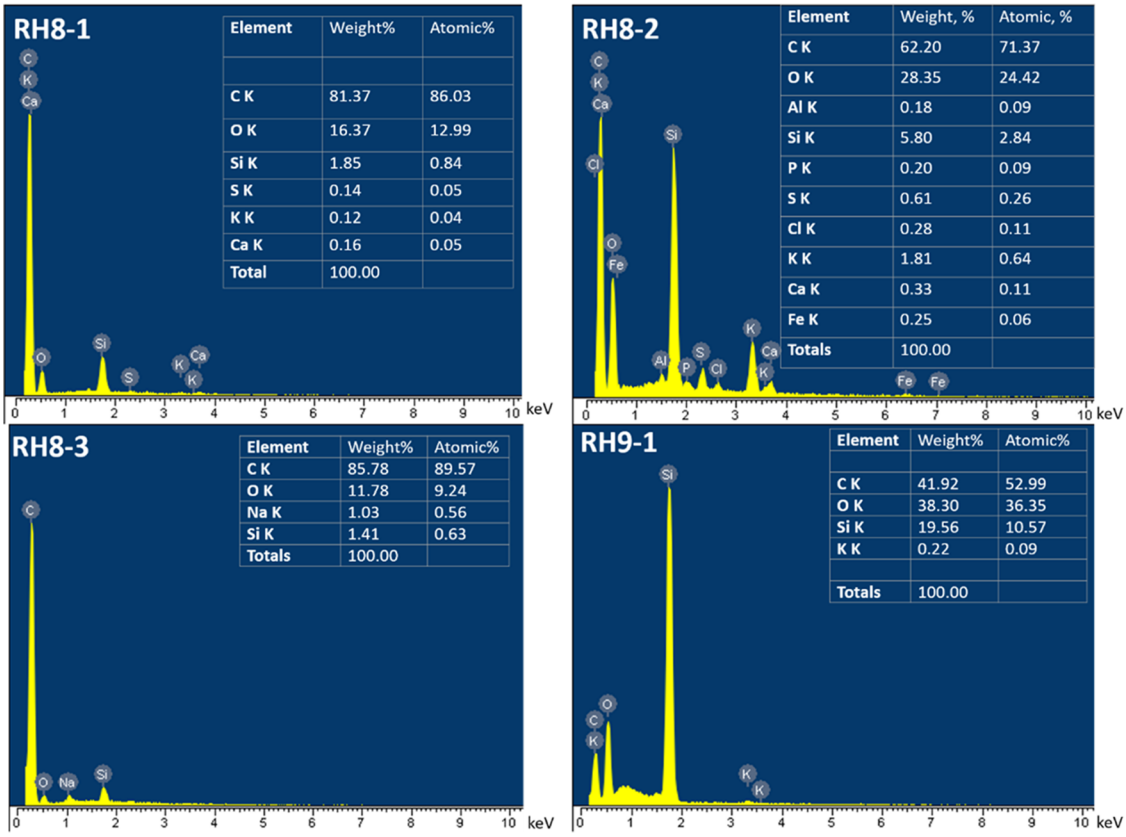

Figure 3. Energy dispersive X-ray spectroscopy (EDX) results of RH8-1, RH8-2, RH8-3, and RH9-1.

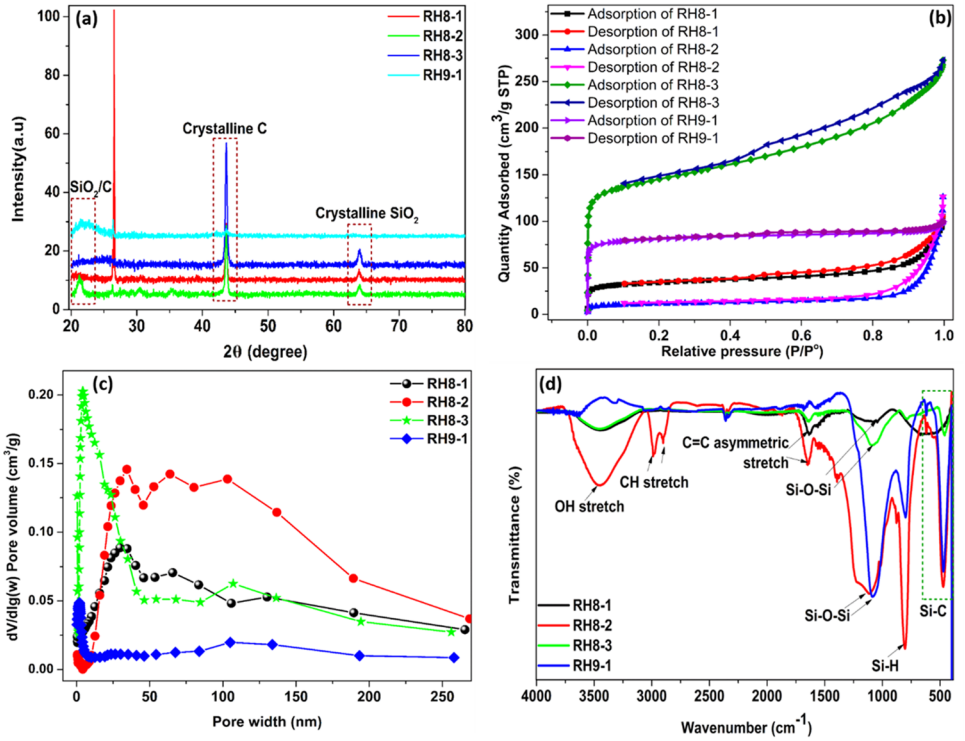

Figure 4. (a) XRD pattern, (b) N_2 adsorption−desorption isotherm, (c) pore size distribution curve, and (d) FT-IR spectra of RH8-1, RH8-2, RH8-3, and RH9-1.

diffusion, and Elovich models and their linear forms. The data are calculated from the following equations given below

$$\log(q_e - q_t) = \log q_e - \frac{t}{2.303}k_1 \quad (11)$$

https://doi.org/10.1021/acsomega.2c07034
ACS Omega 2023, 8, 9904−9918

where k_1 (min^{-1}) is the pseudo-first-order rate constant and t (min) is the contact period.

The pseudo-second-order model is obtained from the equation

$$\frac{t}{q_t} = \frac{1}{k_2 q_e^2} + \frac{1}{q_e} t \quad (12)$$

where k_2 (g mg^{-1} min^{-1}) is the pseudo-second-order rate constant.

The Weber−Morris intraparticle diffusion model is given by

$$q_t = k_3 t^{1/2} + C' \quad (13)$$

where k_3 (mg g^{-1} $min^{-1/2}$) is the intraparticle diffusion rate constant and C' is the intercept.

The Elovich model is given by

$$q_t = \frac{1}{\beta} \ln(\alpha\beta) + \frac{1}{\beta} \ln t \quad (14)$$

where α (mg g^{-1} min^{-1}) is the initial rate of adsorption and β is the adsorption constant.

Moreover, thermodynamic parameters, including $\Delta H°$(enthalpy), $\Delta G°$ (Gibb free energy), and $\Delta S°$ (entropy), are mainly used to determine the spontaneity, feasibility, and nature of interactions between RR120 and the surface of RHs. The mathematical relations are given below

$$\Delta G° = -RT \ln K_d \quad (15)$$

where R is the gas constant (R = 8.314 J K^{-1} mol^{-1}) and T is Kelvin temperature (K).

$$K_d = q_e / C_e$$

$$\Delta G° = \Delta H° - T\Delta S° \quad (16)$$

2.4. Sample Characterization. The surface morphology of RH materials was characterized by scanning electron microscopy (SEM-Hitachi SU8000). The RH materials were also characterized by X-ray diffraction (D2 Phaser Bruker) and Raman spectra (HORIBA, RAM Lab HR 800). The specific surface area and pore size distribution were recorded using N_2 adsorption−desorption isotherms at 77 K (TriStar-300). The chemical composition of the RH was determined by X-ray photoelectron spectroscopy (XPS, Thermo Fisher Scientific, ESCALAB Xi+).

3. RESULTS AND DISCUSSION

3.1. Material Characterization. Figure 2 displays the morphology of RH at various times and temperatures. It could be seen that the burning time affected considerably the morphology of the obtained materials. With a very fast burning of 5 min, RH8-3 exhibited a porous structure with a pore diameter of several micrometers on the surface. However, when the burning time was increased to 2 h for RH8-1 and 8 h for RH8-2, although the temperature was kept constantly at 800 °C, the SiO_2 particles were implanted in carbon nanoplates and no pores were observed. In addition, the burning temperature also had a significant influence on the morphology of RH. It was clear that at the same burning time (RH8-3 and RH9-1), no porous structure could be observed in RH9-1, and the ratio of SiO_2 increased significantly when the temperature increased from 800 to 900 °C (Figure 3). This could be explained to be due to the complete carbon burning of RH at high temperatures to form CO_2.

Table 2. BET Surface Area and Total Pore Volume of RH8-1, RH8-2, RH8-1, and RH9-1

sample name	BET surface area (m^2 g^{-1})	total pore volume of micropores (cm^3 g^{-1})	total pore volume of mesopores (cm^3 g^{-1})	total pore volume (cm^3 g^{-1})
RH8-1	123.38	0.2814	0.9320	1.9984
RH8-2	39.98	0.0908	0.4658	1.9840
RH8-3	521.35	0.5059	3.9931	5.2196
RH9-1	303.37	0.3992	0.6791	1.2252

The impact of both factors on EDX spectra and the elemental composition of the four samples are shown in Figure 3. Obviously, C, O, and Si were the major components of all samples. The carbon content of RH8-3 was the highest at 85.78%, which decreased slightly to 81.37% for RH8-1 when the burning time increased from 5 min to 2 h. On the contrary, the Si content of RH8-1 (1.85%) was higher than that of RH8-3 (1.41%). The carbon content declined dramatically to 62.2% (RH8-2) and 41.92% (RH9-1) when the burning time or temperature greatly increased. However, the Si contents of these two samples increased considerably to 5.8 and 19.56%, respectively. These results demonstrated that the contents of C and Si could be tailored by controlling the burning time and temperature during rice husk burning.

XRD patterns of the materials are illustrated in Figure 4a. XRD spectra of RH8-2 and RH9-1 had a broad peak at a 2θ of 21.7 and 21.26°, respectively, corresponding to the overlapping peak of amorphous carbon and amorphous SiO_2,[31] which was not found in other samples. In addition, a peak at 43.6° with different intensity heights could be observed for all four samples, attributed to the crystalline carbon.[32] Here, the peak intensity of RH8-3 was the highest, demonstrating the high content of carbon, which agreed with EDX data. The peak at 63.92° considering crystalline SiO_2 could be found in RH8-1, RH8-2, and RH8-3.[33] However, it was not available in the XRD pattern of RH9-1, possibly due to its existence in an amorphous state[34] or disappearance at high temperature.

Figure 4b presents the N_2 adsorption−desorption isotherms of the four obtained materials. It indicated that all isotherms belong to type II, which is indicative of macroporous and microporous materials.[35] According to the IUPAC classification, the prepared RH could be considered mesoporous materials because the pore sizes were focused mainly in the range of 2−50 nm as observed in Figure 4c.[36] Also, the open hysteresis loop from the curves of the N_2 isotherm at low $P/P° < 0.2$ confirmed the existence of the mesopores again. In conclusion, the RH series in this report illustrated a good two-dimensional nanoporous structure containing mesopores and micropores. The specific surface area of RH8-3 calculated by the Brunauer−Emmett−Teller (BET) model was 521.35 m^2 g^{-1} with a pore volume of 5.2196 cm^3 g^{-1} and a total pore volume of mesopores (pore sizes range from 1.7 to 23 nm according to the Barrett−Joyner−Halenda (BJH) method)[37] of 3.9931 cm^3 g^{-1}, which were much higher than those of RH8-1, RH8-1, and RH9-1 (Table 2). In the previous work, it was concluded that a large volume of micropores and mesopores should increase pollutant diffusion through internal pores.[38] Thus, it was very beneficial for the electrode materials of supercapacitors/LIBs[7,23] or effective adsorbents for the removal of pollutants in aqueous solutions.

https://doi.org/10.1021/acsomega.2c07034
ACS Omega 2023, 8, 9904−9918

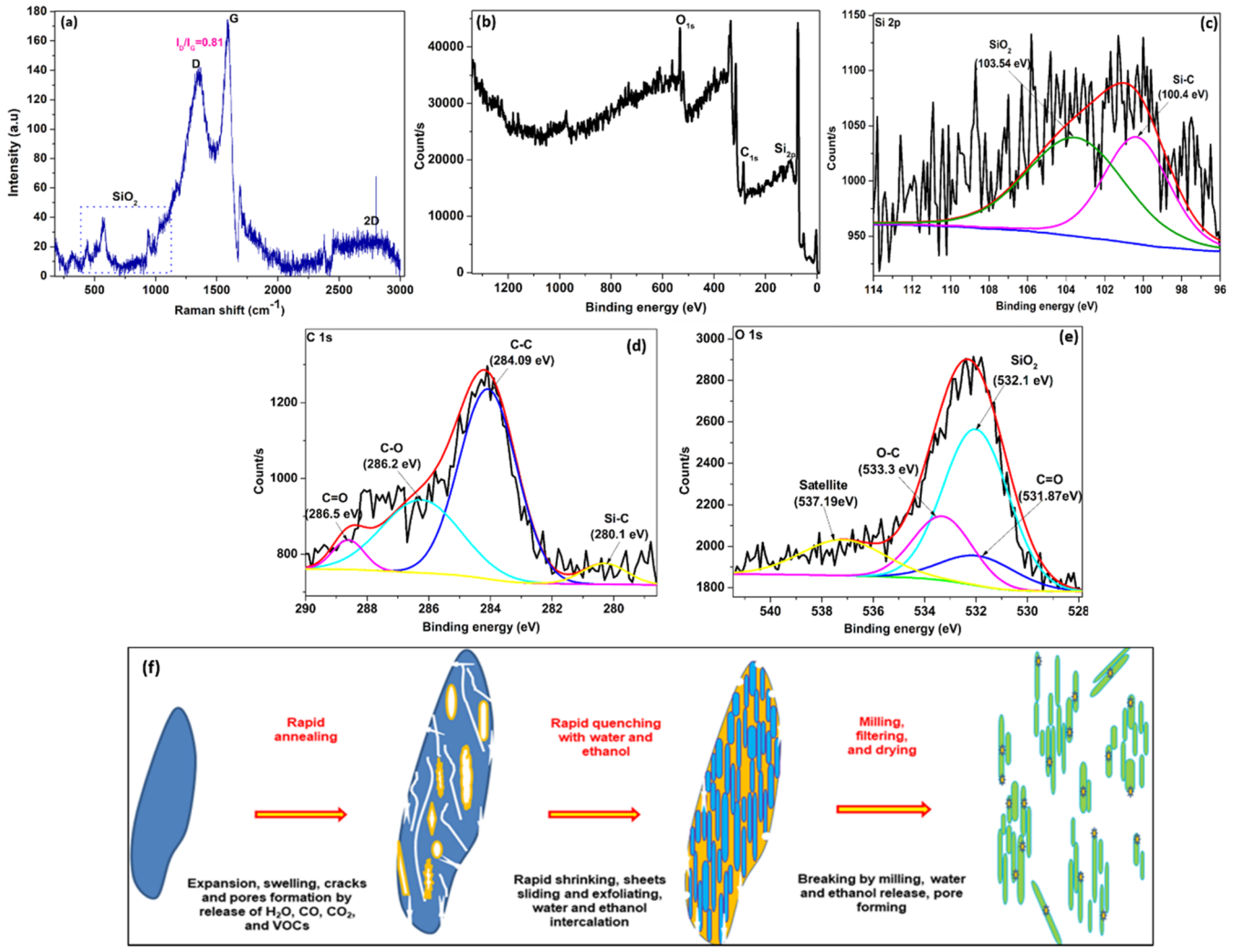

Figure 5. (a) Raman scattering spectrum and XPS spectra of (b) survey, (c) Si 2p, (d) C 1s, (e) O 1s, and (f) the proposed mechanism for the formation of RH8-3.

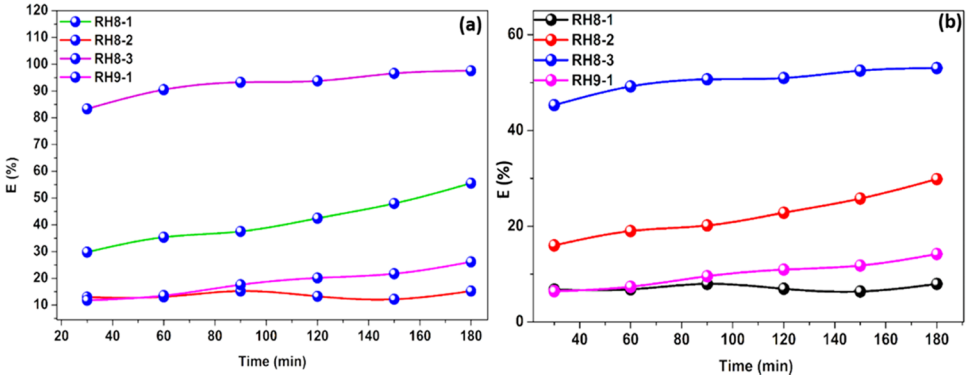

Figure 6. Effect of adsorbent types on removal efficiency (a) and adsorbed capacity (b) (C = 55.00 g L^{-1}, V = 50 mL, T = 298 K, stirring speed = 200 rpm, RH8-3 = 0.03 g, pH = 2.03).

The presence of functional groups was also affirmed by FT-IR spectra as illustrated in Figure 4d. The peaks at around 3456 cm^{-1} (−OH stretch), 2992−2901 cm^{-1} (−CH stretch), and 1674−1640 cm^{-1} (C═C asymmetric stretch) correspond to the typical groups of cellulose, hemicellulose, and lignin of rice husk. In addition, it also could be observed that the peaks at 1109−1055 cm^{-1} are attributed to the Si−O−Si group, while a signal of Si−H is exhibited at 800−790 cm^{-1} and the Si−C stretch group appears at 471−457 cm^{-1}.[39−41] These data demonstrated that the obtained materials were SiO_2@C composites. Additionally, the peak intensities of Si−O−Si, Si−C, and Si−H of RH8-2 and RH9-1 were relatively higher than the others, which agrees with the EDX data.

The above-mentioned results proved that RH8-3 would be a dominant material with a porous structure, high BET surface area, high total pore volume, and mesoporous solid and contain

https://doi.org/10.1021/acsomega.2c07034
ACS Omega 2023, 8, 9904−9918

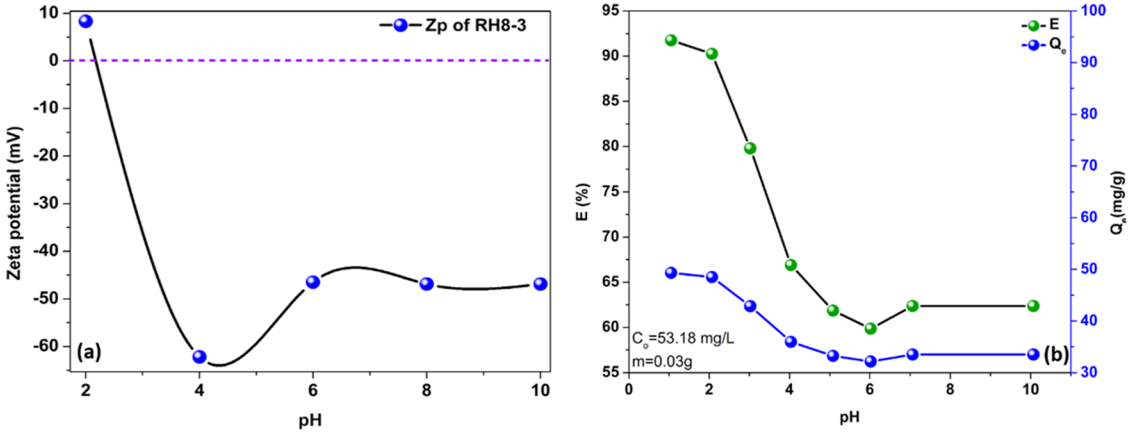

Figure 7. (a) ζ-potential of RH8-3 and (b) effect of pH on the adsorption of RR120 on RH8-3 (V = 50 mL, T = 298 K, stirring speed = 200 rpm).

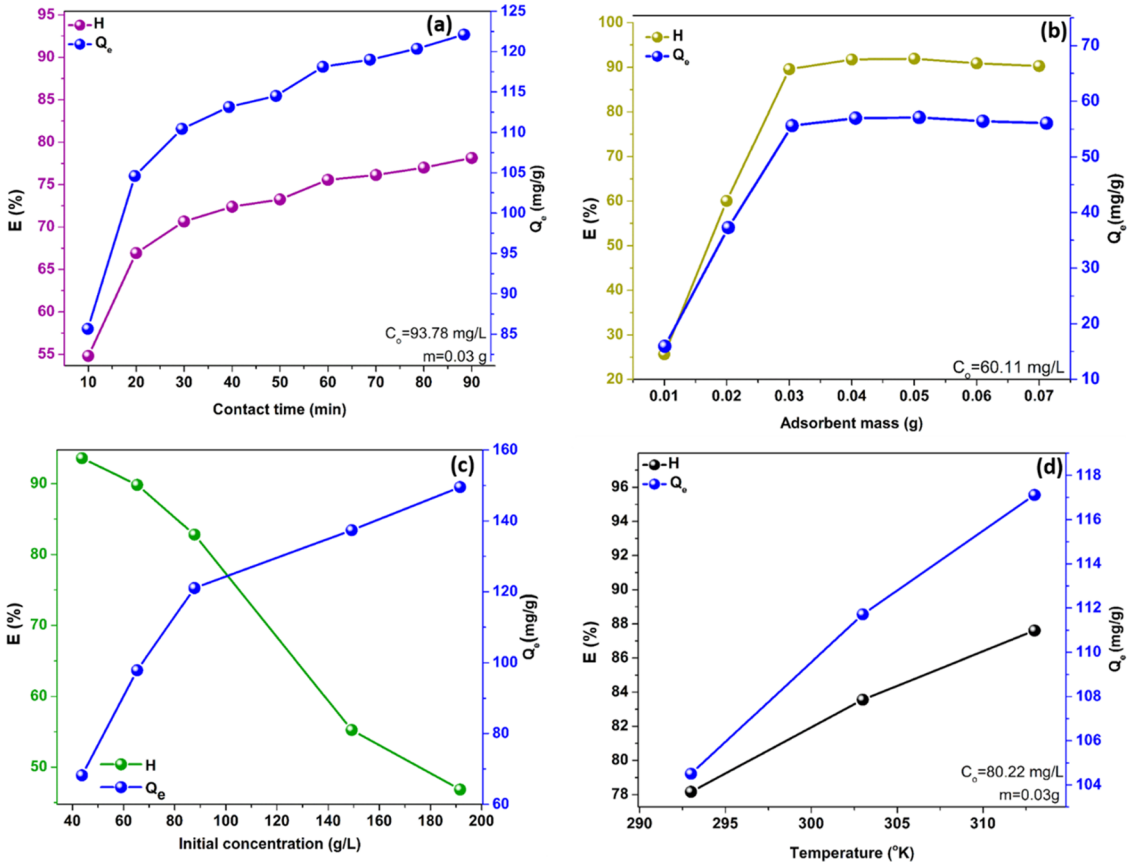

Figure 8. Effect of (a) contact time, (b) adsorbent mass, (c) initial concentration, and (d) temperature on the removal and adsorbed amount of RR120 on RH8-3.

Table 3. Thermodynamic Parameters for the Adsorption of RR120 on RH8-3

temperature (K)	$\Delta G°$ (kJ mol^{-1})	$\Delta H°$ (kJ mol^{-1})	$\Delta S°$ (J mol^{-1} K^{-1})
293	−4351.3266	25 915	103.3
303	−5382.2075		
313	−6417.2519		

SiO_2 particles implanted in the C substrate, suggesting the potential of the material as an adsorbent for the removal of dye pollutants. To further evaluate, Raman spectra, XPS, and the fabrication mechanism of RH8-3 characteristics were performed (Figure 5).

The Raman spectrum (Figure 5a) indicates the characteristic peaks at around 1353 cm^{-1} (D-band) considering amorphous carbon structures and 1589 cm^{-1} (G-band), indicating graphite carbon structures with an I_D/I_G ratio of 0.81.[42−45] However, the intensity of the G-band is higher than that of the D-band, indicating a relatively higher graphitized content in the sample. Notably, the appearance of small peaks at around 441 and 577 cm^{-1} was attributed to the bending vibration of Si−O−Si bonds. The peak at 786 cm^{-1} was considered the symmetric stretching vibration of Si−O−Si, and the band with a peak at 945 cm^{-1} was ascribed to the transverse optical asymmetric stretching vibration of the Si−O−Si bond or/and Si−O−C units, all

https://doi.org/10.1021/acsomega.2c07034
ACS Omega 2023, 8, 9904−9918

Table 4. Kinetic Parameter Calculated for RR120 Adsorption onto RH8-3

model	parameters	unit	values
pseudo-first order (PFO)	k_1	min^{-1}	0.0320
	q_e	$mg\ g^{-1}$	29.0215
	R^2		0.9305
pseudo-second order (PSO)	k_2	$mg\ g^{-1}\ min^{-1}$	0.0016
	q_e	$mg\ g^{-1}$	136.6120
	R^2		0.9982
intraparticle diffusion	k_3	$mg\ g^{-1}\ min^{-1/2}$	4.2269
	C'	$mg\ g^{-1}$	92.3353
	R^2		0.9628
Elovich	α	$mg\ g^{-1}\ min^{-1}$	4814.496
	β	$mg\ g^{-1}$	0.0800
	R^2		0.9734

related to amorphous SiO_2.[46−48] This result was consistent with the XRD and FTIR results. From the above-mentioned characterizations, it could be suggested that the combination of fast annealing and quenching successfully produced the SiO_2/C material with a highly porous structure. We suspect that the formation of SiO_2 confined in the hard carbon frame is due to the incomplete burning of rice husk during the fast fabrication of the material. While conventional porous SiO_2/C nanostructure production usually requires complicated equipment, high-cost and toxic precursors, template precursors, and a multistep synthetic process, this technique is simpler and more efficient for large-scale production.

The elemental composition of RH8-3 was confirmed by the XPS survey results, as exhibited in Figure 5b, showing the main components of C, O, and Si. For Si 2p (Figure 5c), peaks at 100.4 and 103.54 eV could be ascribed to Si−C and SiO_2 bonds, respectively,[49] whereas the peaks at 280.1, 284.09, 286.2, and 288.67 eV are attributed to C−Si, C−C, C−O, and C═O bonds, respectively (Figure 5d).[50,51] Finally, peaks at 531.87, 532.10, 533.3, and 537.1 eV are assigned to the bonds of C═O, SiO_2, C−O, and satellite, respectively (Figure 5e). However, the data for Si 2p were too noisy to determine the existence of oxidized Si of RH8-3, which might be explained due to the low elemental percentage of Si within RH8-3 as exhibited in EDX data. These results are likely that the rapid pyrolysis and quenching of rice husk are an effective method for the formation of RH8-3 containing Si, C, and O as main elements.

Figure 5f illustrates the proposed mechanism of RH8-3 production with four main steps, pointing out a better understanding of the flash pyrolysis mechanism. First, the initial rice husk is annealed up to 800 °C in a short time. The sudden change in temperature inside the reactor causes a thermal shock phenomenon, which results in the swelling of the rice husk structure because of the evaporation of water and volatile organic compounds. The residence time reaction is within 5 min, which can avoid secondary or unwanted reactions. Due to the heating, the carbon generated immediately does not have enough time to grow further and is trapped when cooled rapidly, leading to the formation of carbon nanoplates surrounded by the SiO_2 nanoparticles. In the next step of immediate quenching, the cracks and voids might be filled and intercalated by water.

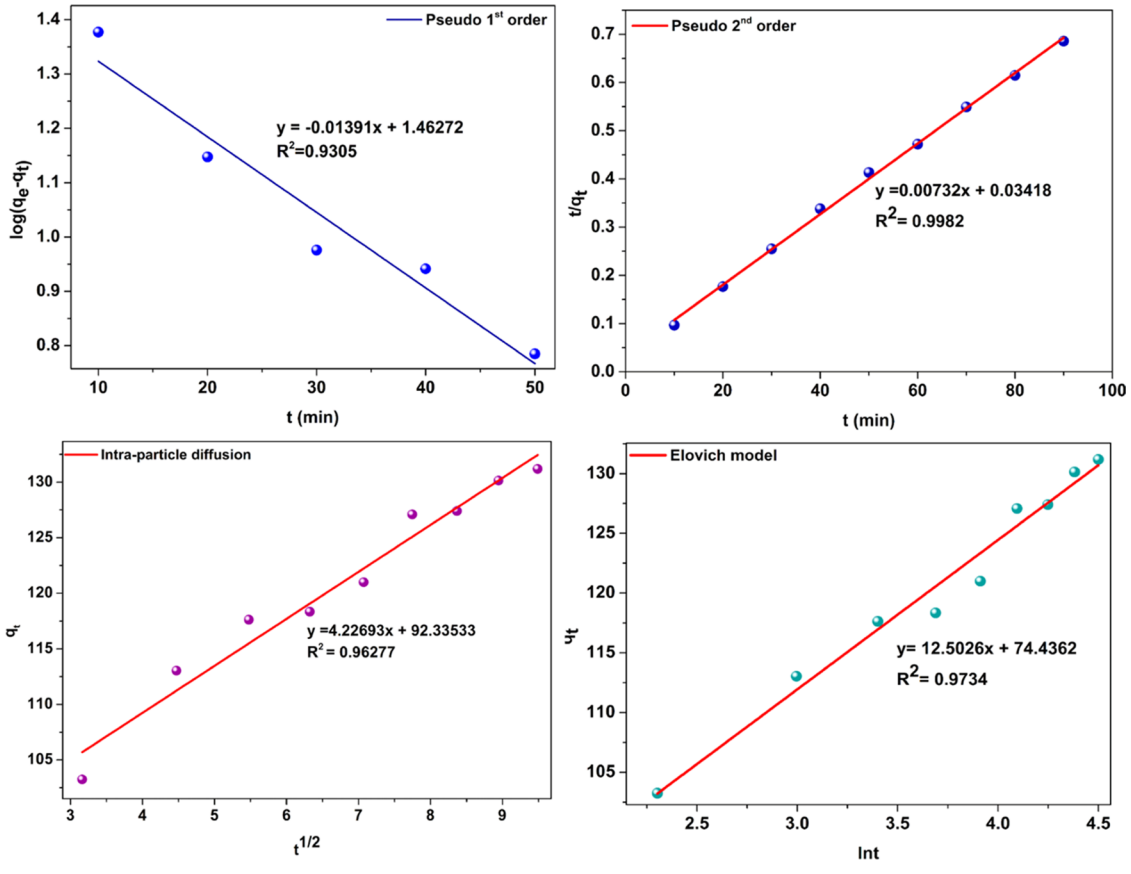

Figure 9. Adsorption kinetics of the PFO, PSO, intraparticle diffusion, and Elovich models of RR120 adsorption.

https://doi.org/10.1021/acsomega.2c07034
ACS Omega 2023, 8, 9904−9918

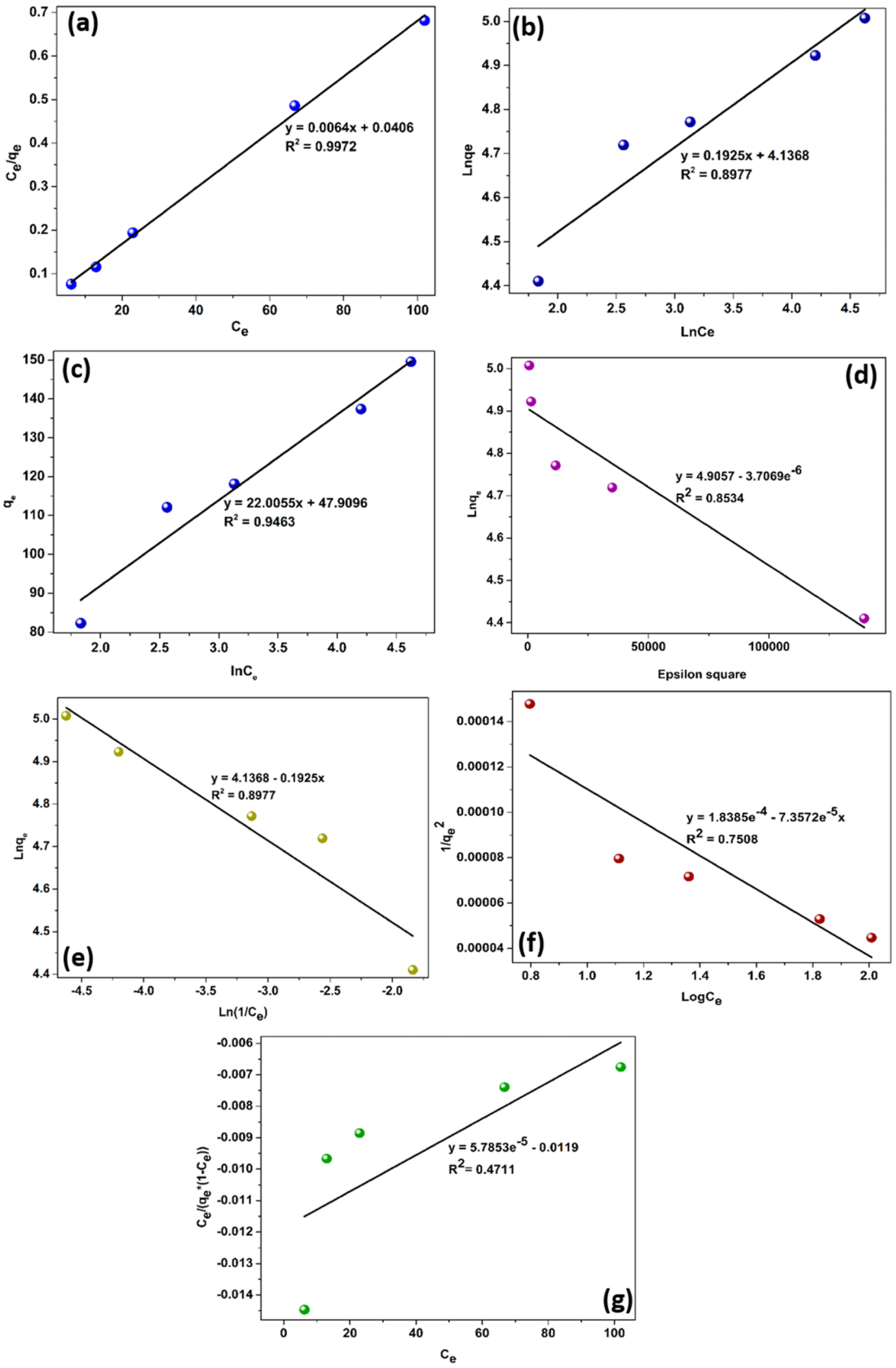

Figure 10. (a) Langmuir, (b) Freundlich, (c) Temkin, (d) Dubinin–Radushkevich, (e) Halsey, (f) Harkins–Jura, and (g) BET models.

Finally, the porous structure is formed through the steaming of water and ethanol during drying.

3.2. RR120 Adsorption by RH8-3. The effect of adsorbents on the removal and adsorbed capacity was investigated (Figure 6). It was clear that after 180 min of treatment, the adsorption

https://doi.org/10.1021/acsomega.2c07034
ACS Omega 2023, 8, 9904−9918

Table 5. Parameters of Isotherm Models

isotherms	equation	parameters	values
Langmuir	$y = 0.0064x + 0.0406$	q_{max}	156.25
		K_L	0.1576
		R_L	0.032
		R^2	0.9972
Freundlich	$y = 0.1925x + 4.1368$	K_F	62.6022
		n	5.1948
		R^2	0.8977
Temkin	$y = 22.0055x + 47.9096$	b_T	114.4778
		a_T	8.8216
		R^2	0.9463
D−R	$y = 4.9057x - (3.7069 \times 10^{-6})$	q_{D-R}	0.9909
		K	4.9057
		R^2	0.8534
		E (kJ mol^{-1})	−0.3193
Halsey	$y = 4.1368 - 0.1925x$	n	
		k	
		R^2	0.8977
Harkins−Jura	$y = (1.8385 \times 10^{-4}) - (7.3572 \times 10^{-5})x$	A	20.1735
		B	0.6793
		R^2	0.7508
BET	$y = (5.7833 \times 10^{-5})x - 0.0119$	q_{max}	36.9443
		k	−2.2746
		R^2	0.4711

Table 6. Comparison of q_{max} Values Achieved from RH8-3 and Other Adsorbents

materials	pH	contact time (min)	q_{max} (mg g^{-1})	refs
RH8-3	2	60	151.52	this work
activated carbon	2	60	267.2	63
nano-alumina	3	150	65.23	64
Chara contraria	1	30	92.35	65
chitosan/modified montmorillonite beads	5	180	5.6	66
cetylpyridinium-bentonite	3	75	79.36	67

efficiency and capacity decreased dramatically, from 97.59% and 52.11 mg g^{-1} for RH8-3 to 55.53% and 29.82 mg g^{-1} for RH8-1 and 15.23% and 7.94 mg g^{-1} for RH8-2 when the burning time increased, respectively. Similarly, a declining trend was also seen (from 97.59% and 52.11 mg g^{-1} for RH8-3 to 26.14% and 14.19 mg g^{-1} for RH9-1) when the temperature increased from 800 to 900 °C. Moreover, since both adsorption efficiency and capacity of RH8-3 did not significantly change between 90 to 180 min of adsorption, the contact time of 90 min was properly the time of equilibrium and was chosen for the following experiments.[52−54] Based on the results, it can be concluded that RH8-3 was a better adsorbent for RR120 in comparison with other samples. Therefore, RH8-3 was used to examine the impact of pH, contact time, adsorbent dosage, concentration, and temperature on RR120 adsorption.

Solution pH value is one of the most important factors governing the adsorption process due to the change in the ζ-potential values of RH8-3 in water with different pH values (Figure 7a). The surface of RH8-3 was negatively charged in the pH values from 3.0 to 10.0 due to its point of zero charge (pHpzc) of 2.16 < 3. Interestingly, the potential value changed greatly from −62.14 to 8.56 mV with a decrease in pH from 4.0 to 2.0.

The adsorption efficiency and capacity of RR120 by RH8-3 are illustrated in Figure 7b. It was obvious that both the efficiency and capacity of RR120 adsorption by RH8-3 were maximum at pH < 2.16. It can be explained that the sulfonate group from RR120 is dissociated and converted to anionic dye ions in an aqueous solution as expressed in the equation

$$RR120 - SO_3Na \leftrightarrow RR120 - SO_3^- + Na^+$$

Thus, RR120 was negatively charged, while RH8-3 was positively charged at pH < 2.16, as illustrated in Figure 7a. Therefore, the adsorption process between the dye molecules and adsorbent occurs by electrostatic forces as well as intraparticle and surface diffusion. However, when the pH values increased, the adsorption efficiency and capacity declined dramatically due to the repulsion between anionic ions and the adsorbent surface.[55,56]

The time dependence of RR120 adsorption is presented in Figure 8a. As can be seen, the adsorption efficiency and capacity of RH8-3 depend on the contact time. Obviously, the adsorption of RR120 on RH8-3 occurred quickly with more than 50% of RR120 in the aqueous solution adsorbed within 30 min of contact. In general, the adsorption capacity of RR120 increased consecutively during the initial 45 min of contact and subsequently reached the highest efficiency at 90 min.

Figure 8b exhibits the influence of the adsorbent dosage on the adsorption capacity. It was found that by increasing the RH8-3 dosage up to 0.03 g, the adsorption efficiency and capacity increased quickly, which were then not affected significantly by the further addition of the RH8-3. The increase

https://doi.org/10.1021/acsomega.2c07034
ACS Omega 2023, 8, 9904−9918

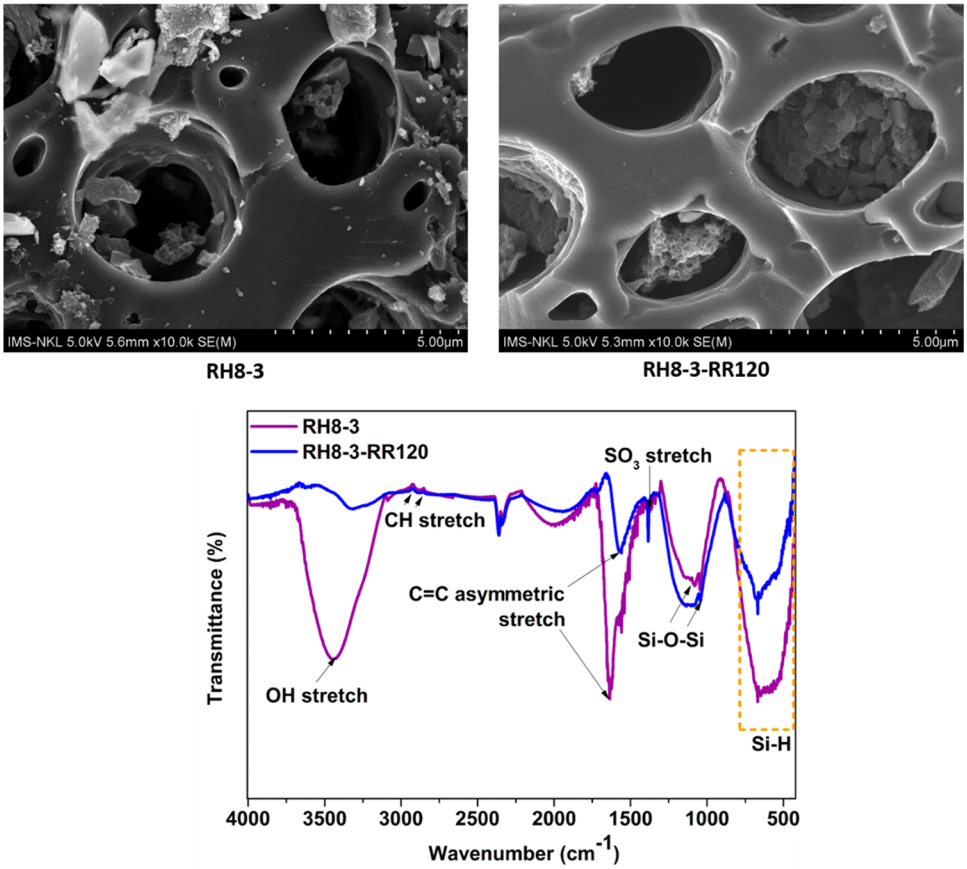

Figure 11. SEM images and FT-IR spectra of RH8-3 before and after adsorption.

in the RR120 adsorption with the RH8-3 dosage was attributed to the large adsorbent surface area as well as the increase in the number of adsorption centers. However, no significant changes in RR120 adsorption were seen beyond 0.03 g of RH8-3 dosage due to the reaching of adsorption equilibrium with a fixed amount of RR120. Therefore, 0.03 g of RH8-3 was chosen for the next experiments.

Figure 8c illustrates the effect of the RR120 initial concentration on the adsorption efficiency and capacity. It is clear that the adsorption capacity of RH8-3 increased with the increase of the initial concentration of RR120. The highest adsorption capacity of RR120 was obtained with 191.62 ppm RR120 initial concentration. Higher uptake at higher initial concentrations may occur because of the higher driving force formation by the mass gradient between solutions and the adsorbent surface, which leads to higher quantities of RR120 molecules being transferred to the RH8-3 surface. However, the reserve trend was observed with the RR120 adsorption efficiency, which happened due to the filling up of the adsorption centers of RH8-3 with too high initial concentrations of RR120.

The influence of temperature on the adsorption efficiency and capacity is indicated in Figure 8d. It is obvious that the RR120 adsorption increased with increasing temperature. This can be explained that when the adsorption temperature increased, the mobility of RR120 molecules also increased, so the adsorption also increased. Thus, it can be concluded that the adsorption of RR120 on the RH8-3 material is an endothermic process. This is also confirmed by adsorption thermodynamic parameters as shown in Table 3. According to Table 3, the negative value of Gibbs free energy ($\Delta G < 0$) indicates that the adsorption RR120 on RH8-3 was a spontaneous physical state, while a positive value of enthalpy ($\Delta H > 0$) exhibited the heat required for the adsorption system. These denote that the adsorption phenomenon was endothermic, and the positive value of entropy ($\Delta S > 0$) demonstrates an increase of the disorder at the solution/adsorbent interface during the adsorption of RR120 on RH8-3.[57]

In addition, the adsorption reaction was correlated by four kinetic models, including pseudo-first-order (PFO), pseudo-second-order (PSO), intraparticle, and Elovich kinetic models, with the parameters displayed in Table 4 and Figure 9. It can be noted that the PSO model gave the highest value of the coefficient of determination (R^2) in comparison to that of the PFO, the intraparticle diffusion, and the Elovich models. Therefore, the PSO kinetic model fitted better the experimental result of adsorption. It means that RH8-3 possessed a strong affinity to RR120 in aqueous media, and the adsorption kinetics was favorable with adsorption onto active sites.[58] Additionally, the rate of the adsorption equilibrium of RR120 onto RH8-3 (k_2) was 0.0016 mg g^{-1} min^{-1}. This shows a tendency toward physisorption, implying that the interaction between the electrostatic forces of RR120-SO_3^- ions and the surface of the adsorbent was similar to the mechanism reported by refs 59 and 60. Based on the PSO equation, the equilibrium adsorption capacity was 136.612 mg g^{-1}, which was much bigger than those for other models.

Additionally, to describe the adsorption onto active sites, Langmuir, Freundlich, Temkin, Dubinin−Radushkevich, Halsey, Harkins−Jura, and BET models were used.[61,62] The results are illustrated in Figure 10, while the calculated parameters are

https://doi.org/10.1021/acsomega.2c07034
ACS Omega 2023, 8, 9904−9918

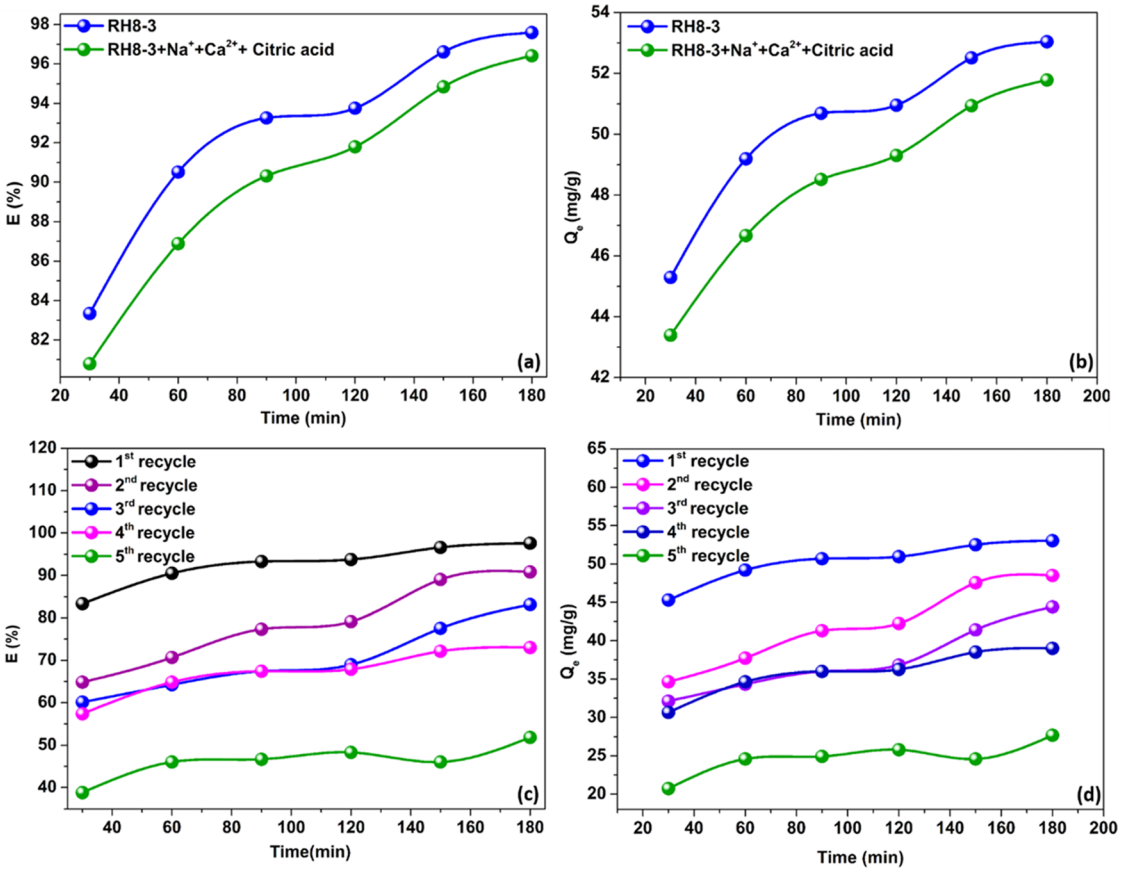

Figure 12. Effect of coexisting organic (a) and inorganic (b) materials and the number of recycling times on the effectiveness (c) and adsorbed capacity (d) of RR120 by RH8-3.

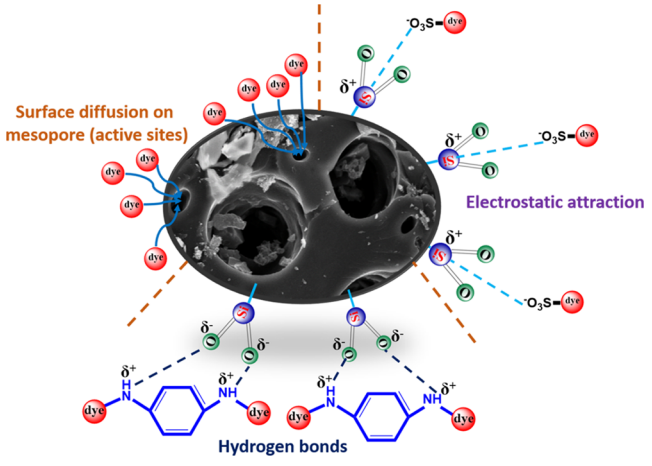

Figure 13. Possible mechanism of RR120 adsorption on RH8-3.

shown in Table 5. The R^2 parameter (indicated in parentheses) for each model was in the order Langmuir isotherm (0.9972) > Temkin isotherm (0.9463) > Freundlich isotherm (0.8977) and Hasley isotherm (0.8977) > Dubinin−Radushkevich isotherm (0.8534) > Harkins−Jura isotherm (0.7508) > BET isotherm (0.4711). This suggests that the Langmuir isotherm is the best for fitting the experimental data, indicating the adsorption of RR120 as a monolayer on the homogeneous surface of RH8-3 and each active site of RH8-3 providing the same affinity for the adsorbate molecules. From Table 5, the R_L value was calculated by replacing the K_L value in the equation $R_L = 1/(1 + K_L \times C_o)$, where C_o is the highest initial solute concentration. The value of $0 < R_L = 0.02 < 1$ illustrates that the physical adsorption process was favorable. Several RR120 molecules are adsorbed on the active sites via electrostatic attractions and hydrogen bonding or intraparticle diffusion and surface diffusion. Thus, it can be concluded that on the surface of RH8-3, there was monolayer adsorption on various active sites by physisorption. In addition, the maximum adsorption capacity (q_{max}) of RR120 on RH8-3 was calculated from the Langmuir equation. The result of q_{max} was 156.25 mg g^{-1}, which is higher than those obtained from other models as shown in Table 5. For comparison, the q_{max} values of the RR120 dye on the RH8-3 and some other adsorbents in the previous literature are summarized in Table 6. As expected, RH8-3 exhibited a reasonably higher q_{max} value than that of most other adsorbents in the literature. Therefore, it was foreseen that the porous carbon derived from rice husk can serve as a promising adsorbent for the treatment of water containing colored substances.

3.3. Stability of the Prepared Adsorbent. The influence of pH, reusability, and coexisting organic and inorganic materials on the adsorption of RR120 by RH8-3 was then considered. Figure 11 shows the effect of pH on the stability of the adsorbent. Before adsorption, RH8-3 had a porous structure with a diameter of several micrometers, which was kept stable after the adsorption of RR120. As can be seen in FT-IR analysis, the peak at 3456 cm^{-1} (presence of the OH stretch group) was shifted slightly to 3335.33 cm^{-1} after binding RR120. The peaks at around 2992.30 and 2853.33 cm^{-1} showed the existence of the CH stretch in both RH8-3 and RH8-3-RR120. Similarly, the peak at 1636.05 cm^{-1} for the C═C asymmetric stretch

https://doi.org/10.1021/acsomega.2c07034
ACS Omega 2023, 8, 9904−9918

decreased softly to 1566.94 cm^{-1} when RR120 was absorbed on the RH8-3 surface. However, there were new peaks at 1384.62 cm^{-1}, corresponding to the SO_3 stretch groups,[68,69] which were absent in the spectra of the native RH8-3. Moreover, the peaks observed at 1080 and 1083 cm^{-1} attributed to the Si−O−Si stretch and 658.91 and 663.68 cm^{-1} attributed to Si−H can be seen in both RH8-3 and RH8-3 after RR120 adsorption. Therefore, the SEM images and FT-IR spectra proved that the structure and functional groups of RH8-3 were kept stable after the adsorption process at intensive pH.

Additionally, the effect of the coexisting organic and inorganic materials and the number of recycles for the adsorption of RR120 by RH8-3 were also characterized. As can be seen in Figure 12, the adsorption declined slightly from 97.59% and 53.04 mg g^{-1} for RR120 to 96.41% and 51.78 mg g^{-1} for RR120 with other components with the presence of Na^+, Ca^{2+}, and citric acid. In addition, the effectiveness decreased slowly from 97.59 to 90.81, 83.14, 73.02, and 51.80% after using the material five times. Similarly, the adsorption capacity also reduced from 53.04 to 48.49, 44.40, 38.99, and 27.66 mg g^{-1}. These results proved that the stability of RH8-3 was high, although the adsorbent was used at a very intensive pH and the appearance of other components had little impact on adsorption.

3.4. Adsorption Mechanisms. According to the analytical results from the ζ-potential, isotherm, and kinetic models, the adsorption mechanism of RR120 on RH8-3 is proposed in Figure 13. As discussed in the ζ-potential section, RR120 was dissociated into RR120-SO_3^- and Na^+ in an aqueous solution. At the same time, the surface of RH8-3 was charged positively at pH 2. Thus, the adsorption process occurred by the electrostatic attraction between $Si^{\delta+}$ on the surface of RH8-3 and SO_3^- of RR120.[70] However, a significant amount of RR120 being adsorbed still occurred at higher pH values (pH > 2), although the highly negative surface of RH8-3 was not beneficial for the adsorption due to electrostatic repulsion. Thus, other adsorption mechanisms rather than electrostatic interaction are responsible for the RR120 adsorption by RH8-3.[71] In this case, RR120 adsorption onto RH8-3 could be partly attributed to hydrogen bonds among −NH groups of RR120 and O of SiO_2 on the surface of the adsorbent, which was illustrated by the shift of the −OH peak from 3456 to 3335.33 cm^{-1} and the intensity increase in the −NH peak at 2361.75 cm^{-1} (Figure 11). In addition, the results from the Langmuir isotherm and pseudo-second-order model also demonstrated that the adsorption of RR120 on the RH8-3 surface takes place as a monolayer by diffusion of dye molecules onto active sites on the surface of the mesopores.[72]

4. CONCLUSIONS

The biomass rice husk-derived porous SiO_2/C nanocomposites were successfully prepared via rapid annealing, quenching, and grinding techniques with a high surface area of 521.35 m^2 g^{-1} and a large pore volume of 5.2196 cm^3 g^{-1}. The results confirmed that at pH 2, a contact time of 90 min, an adsorbent dosage of 0.03 g, an RR120 initial concentration of approx. 93.78 mg L^{-1}, and a temperature of 40 °C, around 93% of RR120 was adsorbed. The Langmuir isotherm was the best-fitted model for the adsorption of RR120 onto RH8-3 with a maximum adsorption capacity of 152.51 mg g^{-1}, whereas the pseudo-second-order one was the most suitable model to describe the equilibrium of the adsorption process. The presence of other compounds also did not affect much the removal and adsorbed amount of RR120 on RH8-3. After recycling five times, the performance still remained at about 51.8% and 27.66 mg g^{-1}. The FT-IR and SEM results also proved that the adsorbent was still stable, although it was applied at a very intensive pH value. Therefore, this novel, simple, and effective technology could provide a clean and sustainable way to utilize rice husk for mass production of SiO_2/C nanocomposites in practical applications.

AUTHOR INFORMATION

Corresponding Authors

Nguyen Thi Thuy − *School of Chemical and Environmental Engineering, International University, Ho Chi Minh City 700000, Vietnam; Vietnam National University Ho Chi Minh City, Ho Chi Minh City 700000, Vietnam;* orcid.org/0000-0002-3736-4313; Phone: +84 903 250 375; Email: ntthuy@hcmiu.edu.vn

Nguyen Thi Mai − *Faculty of Environmental Sciences, University of Science, Vietnam National University, Hanoi, Hanoi 100000, Vietnam; Faculty of Basic Sciences, Thai Nguyen University of Agriculture and Forestry, Thai Nguyen 25000, Vietnam;* orcid.org/0000-0002-1785-4729; Phone: +84 964 070 182; Email: nguyenthimai82@tuaf.edu.vn

Authors

Tran Quoc Toan − *Faculty of Chemistry, Thai Nguyen University of Education, Thái Nguyên 25000, Vietnam*

Tran Kim Ngan − *Faculty of Chemistry, Thai Nguyen University of Education, Thái Nguyên 25000, Vietnam*

Do Tra Huong − *Faculty of Chemistry, Thai Nguyen University of Education, Thái Nguyên 25000, Vietnam*

Phuoc-Anh Le − *Institute of Sustainability Science, VNU Vietnam Japan University, Vietnam National University, Hanoi 10000, Vietnam*

Nguyen Nhat Huy − *Vietnam National University Ho Chi Minh City, Ho Chi Minh City 700000, Vietnam; Faculty of Environment and Natural Resources, Ho Chi Minh City University of Technology (HCMUT), Ho Chi Minh City 70000, Vietnam;* orcid.org/0000-0002-2918-7935

Dang Van Thanh − *Faculty of Basic Science, Thai Nguyen University of Medicine and Pharmacy, Thai Nguyen 25000, Vietnam; Faculty of Environmental Sciences, University of Science, Vietnam National University, Hanoi, Hanoi 100000, Vietnam;* orcid.org/0000-0002-8870-6934

Nguyen Manh Khai − *Faculty of Environmental Sciences, University of Science, Vietnam National University, Hanoi, Hanoi 100000, Vietnam*

Complete contact information is available at: https://pubs.acs.org/10.1021/acsomega.2c07034

Author Contributions

T.Q.T., and T.K.N. carried out the experiments. D.T.H. analyzed data and curated data. D.V.T., N.M.K., N.N.H., and P.A.L. performed review and editing. N.T.M. and N.T.T. conceived, designed, and supervised experiments and wrote the original draft. All authors have read and approved the final article.

Funding

This work was supported by the Ministry of Education and Training of Vietnam (grant no. B2021-TNA-15, 2021).

Notes

The authors declare no competing financial interest.

https://doi.org/10.1021/acsomega.2c07034
ACS Omega 2023, 8, 9904−9918

REFERENCES

(1) Manogaran, M.; Yasid, N. A.; Othman, A. R.; Gunasekaran, B.; Halmi, M. I. E.; Shukor, M. Y. A. Biodecolourisation of Reactive Red 120 as a sole carbon source by a bacterial consortium—Toxicity assessment and statistical optimisation. *Int. J. Environ. Res. Public Health* **2021**, *18*, No. 2424.

(2) Robinson, T.; McMullan, G.; Marchant, R.; Nigam, P. Remediation of dyes in textile effluent: a critical review on current treatment technologies with a proposed alternative. *Bioresour. Technol.* **2001**, *77*, 247−255.

(3) Khataee, A.; Alidokht, L.; Hassani, A.; Karaca, S. Response surface analysis of removal of a textile dye by a Turkish coal powder. *Adv. Environ. Res.* **2013**, *2*, 291−308.

(4) Van Hao, P.; Minh, P. N.; Hong, P. N.; Huy, N. N.; Oanh, P. T.; Nguyen, H. T.; Tran, T. D.; Van Thanh, D.; Van Dang, N. Gram-scale synthesis of electrochemically oxygenated graphene nanosheets for removal of methylene blue from aqueous solution. *Nanotechnology* **2021**, *32*, No. 16LT01.

(5) Nang An, V.; Chi Nhan, H. T.; Tap, T. D.; Van, T. T. T.; Van Viet, P.; Van Hieu, L. Extraction of High Crystalline Nanocellulose from Biorenewable Sources of Vietnamese Agricultural Wastes. *J. Polym. Environ.* **2020**, *28*, 1465−1474.

(6) Vu, D.-L.; Seo, J.-S.; Lee, H.-Y.; Lee, J.-W. Activated carbon with hierarchical micro−mesoporous structure obtained from rice husk and its application for lithium−sulfur batteries. *RSC Adv.* **2017**, *7*, 4144−4151.

(7) Autthawong, T.; Namsar, O.; Yu, A.; Sarakonsri, T. Cost-effective production of SiO 2/C and Si/C composites derived from rice husk for advanced lithium-ion battery anodes. *J. Mater. Sci.: Mater. Electron.* **2020**, *31*, 9126−9132.

(8) Al Ja'farawy, M. S.; Hikmah, D. N.; Riyadi, U.; Purwanto, A.; Widiyandari, H. A Review: The Development of SiO 2/C Anode Materials for Lithium-Ion Batteries. *J. Electron. Mater.* **2021**, 1−21.

(9) Wang, J.; Xiao, L.; Wen, S.; Chen, N.; Dai, Z.; Deng, J.; Nie, L.; Min, J. Hierarchically porous SiO 2/C hollow microspheres: a highly efficient adsorbent for Congo Red removal. *RSC Adv.* **2018**, *8*, 19852−19860.

(10) Qin, Y.; Li, X.; Wang, L.; Luo, J.; Li, Y.; Yao, C.; Xiao, Z.; Zhai, S.; An, Q. Valuable cobalt/biochar with enriched surface oxygen-containing groups prepared from bio-waste shrimp shell for efficient peroxymonosulfate activation. *Sep. Purif. Technol.* **2022**, *281*, No. 119901.

(11) Qin, Y.; Luo, J.; Zhao, Y.; Yao, C.; Li, Y.; An, Q.; Xiao, Z.; Zhai, S. Dual-wastes derived biochar with tailored surface features for highly efficient p-nitrophenol adsorption. *J. Cleaner Prod.* **2022**, *353*, No. 131571.

(12) Lin, L.; Zhai, S.-R.; Xiao, Z.-Y.; Liu, N.; Song, Y.; Zhai, B.; An, Q.-D. Cooperative effect of polyethylene glycol and lignin on SiO2 microsphere production from rice husks. *Bioresour. Technol.* **2012**, *125*, 172−174.

(13) Chen, Y.; Zhai, S.-R.; Liu, N.; Song, Y.; An, Q.-D.; Song, X.-W. Dye removal of activated carbons prepared from NaOH-pretreated rice husks by low-temperature solution-processed carbonization and H3PO4 activation. *Bioresour. Technol.* **2013**, *144*, 401−409.

(14) Lin, L.; Zhai, S.-R.; Xiao, Z.-Y.; Song, Y.; An, Q.-D.; Song, X.-W. Dye adsorption of mesoporous activated carbons produced from NaOH-pretreated rice husks. *Bioresour. Technol.* **2013**, *136*, 437−443.

(15) Lv, J.-L.; Zhai, S.-R.; Wang, Z.-Z.; Lei, Z.-M.; An, Q.-D. Carbon−silica composite bio-sorbents with a high density of oxygen-containing sites for efficient methylene blue adsorption. *Res. Chem. Intermed.* **2016**, *42*, 839−854.

(16) Fan, Y.; Zhai, S.; Liu, N.; Lv, J.; Lei, Z.; An, Q. Adsorption equilibrium, kinetics and mechanism of Pb (II) over carbon−silica composite biosorbent with designed surface oxygen groups. *Res. Chem. Intermed.* **2016**, *42*, 869−891.

(17) Jiang, X.; An, Q.-D.; Xiao, Z.-Y.; Zhai, S.-R.; Shi, Z. Mussel-inspired surface modification of untreated wasted husks with stable polydopamine/polyethylenimine for efficient continuous Cr (VI) removal. *Mater. Res. Bull.* **2018**, *102*, 218−225.

(18) Hassani, A.; Khataee, A. Carbon Nanomaterials for Removal of Pharmaceuticals from Wastewater. In *Nanomaterials for Water Treatment and Remediation*; CRC Press, 2021; pp 333−369.

(19) Nguyen, T. T.; Padungthon, S.; Nguyen, N. H. Activated rice husk ash-supported silver nanoparticles as a novel adsorbent toward chloride removal. *Desalin. Water Treat.* **2019**, *160*, 308−315.

(20) Phan, P. T.; Nguyen, T. T.; Nguyen, N. H.; Padungthon, S. Triamine-bearing activated rice husk ash as an advanced functional material for nitrate removal from aqueous solution. *Water Sci. Technol.* **2019**, *79*, 850−856.

(21) Molkenova, A.; Taniguchi, I. Preparation and characterization of SiO2/C nanocomposites by a combination of mechanochemical-assisted sol−gel and dry ball milling processes. *Adv. Powder Technol.* **2015**, *26*, 377−384.

(22) Li, D.; Zhang, X.; Wang, Y.; Yan, X.; Zong, P.; Lu, G.; Tian, Y. Activation of rice hull char with steam to improve lithium storage performance of SiO2/C. *J. Anal. Appl. Pyrolysis* **2021**, *157*, No. 105185.

(23) Dawei, L.; Xiaoxiao, Z.; Yu, W.; Peijie, Z.; Li, Z.; Zongbo, Z.; Xin, G.; Yingyun, Q.; Guixia, L.; Yuanyu, T. Adjusting ash content of char to enhance lithium storage performance of rice husk-based SiO2/C. *J. Alloys Compd.* **2021**, *854*, No. 156986.

(24) Xia, H.; Yin, Z.; Zheng, F.; Zhang, Y. Facile synthesis of SiO2/C composites as anode materials for lithium-ion batteries. *Mater. Lett.* **2017**, *205*, 83−86.

(25) Wang, L.; Xue, J.; Gao, B.; Gao, P.; Mou, C.; Li, J. Rice husk derived carbon−silica composites as anodes for lithium ion batteries. *RSC Adv.* **2014**, *4*, 64744−64746.

(26) Tschuncky, R.; Szielasko, K.; Altpeter, I. Hybrid Methods for MMaterials Characterization. In *Materials Characterization Using Nondestructive Evaluation (NDE) Methods*; Elsevier, 2016; pp 263−291.

(27) Dahmen, U. Phase Transformations, Crystallographic Aspects. In *Encyclopedia of Physical Science and Technology*; Academic Press: San Diego, CA, 1986.

(28) Whang, S.-H. *Nanostructured Metals and Alloys: Processing, Microstructure, Mechanical Properties and Applications*; Elsevier, 2011.

(29) Chaus, A. S.; Chovanec, J.; Legerská, M.Development of High-Speed Steels for Cast Metal-Cutting Tools. In *Solid State Phenomena* 2006; pp 559−564.

(30) Van Thanh, D.; Oanh, P. P.; Huong, D. T.; Le, P. H. Ultrasonic-assisted cathodic electrochemical discharge for graphene synthesis. *Ultrason. Sonochem.* **2017**, *34*, 978−983.

(31) Li, D.; Zhang, X.; Wang, Y.; Yan, X.; Zong, P.; Lu, G.; Tian, Y. Activation of rice hull char with steam to improve lithium storage performance of SiO2/C. *J. Anal. Appl. Pyrolysis* **2021**, *157*, No. 105185.

(32) Xiong, L.; Huang, X.; Liu, Y.; Pan, L. One-step preparation and characterization of core-shell SiO2/Ag composite spheres by pulse plating. *Sci. Eng. Compos. Mater.* **2017**, *24*, 423−427.

(33) Yang, R.; Diao, Y.; Abayneh, B. Removal of Hg0 from simulated flue gas over silver-loaded rice husk gasification char. *R. Soc. Open Sci.* **2018**, *5*, No. 180248.

(34) Gao, X.; Zhang, Y.; Xu, F.; Yin, Z.; Wang, Y.; Bao, F.; Li, B. Experimental and kinetic studies on the intrinsic reactivities of rice husk char. *Renewable Energy* **2019**, *135*, 608−616.

(35) Daffalla, S. B.; Mukhtar, H.; Shaharun, M. Sorption of phenol from aqueous solutions using acid-treated rice husk. *WIT Trans. Ecol. Environ.* **2013**, *179*, 1177−1188.

(36) Zulkifli, N. S. C.; Ab Rahman, I.; Mohamad, D.; Husein, A. A green sol−gel route for the synthesis of structurally controlled silica particles from rice husk for dental composite filler. *Ceram. Int.* **2013**, *39*, 4559−4567.

(37) Brunauer, S.; Emmett, P. H.; Teller, E. Adsorption of gases in multimolecular layers. *J. Am. Chem. Soc.* **1938**, *60*, 309−319.

(38) Kruczyński, S. W.; Orliński, P.; Ślęzak, M. NOx Reduction in Ag/Al2O3-SiO2 Converters in the Exhaust of a Compression-Ignition Engine. *Energies* **2021**, *14*, No. 20.

(39) Kaur, P.; Kaur, P.; Kaur, K. Adsorptive removal of imazethapyr and imazamox from aqueous solution using modified rice husk. *J. Cleaner Prod.* **2020**, *244*, No. 118699.

https://doi.org/10.1021/acsomega.2c07034
ACS Omega 2023, 8, 9904−9918

(40) Daffalla, S. B.; Mukhtar, H.; Shaharun, M. S. Preparation and characterization of rice husk adsorbents for phenol removal from aqueous systems. *PLoS One* **2020**, *15*, No. e0243540.
(41) Lawagon, C. P.; Amon, R. E. C. Magnetic rice husk ash'cleanser'as efficient methylene blue adsorbent. *Environ. Eng. Res.* **2020**, *25*, 685−692.
(42) Chen, C.; Yu, D.; Zhao, G.; Du, B.; Tang, W.; Sun, L.; Sun, Y.; Besenbacher, F.; Yu, M. Three-dimensional scaffolding framework of porous carbon nanosheets derived from plant wastes for high-performance supercapacitors. *Nano Energy* **2016**, *27*, 377−389.
(43) Chinnadurai, D.; Rajendiran, R.; Selvaraj, A. R.; Kim, H.-J.; Prabakar, K. Interplay between porous texture and surface-active sites for efficient oxygen reduction reactions in N-inherited carbon. *New J. Chem.* **2020**, *44*, 10911−10917.
(44) Duraisamy, V.; Sudha, V.; Annadurai, K.; Kumar, S. M. S.; Thangamuthu, R. Ultrasensitive simultaneous detection of ascorbic acid, dopamine, uric acid and acetaminophen on a graphitized porous carbon-modified electrode. *New J. Chem.* **2021**, *45*, 1863−1875.
(45) Zhang, W.; Qi, J.; Bai, P.; Wang, H.; Xu, L. High-level nitrogen-doped, micro/mesoporous carbon as an efficient metal-free electrocatalyst for the oxygen reduction reaction: Optimizing the reaction surface area by a solvent-free mechanochemical method. *New J. Chem.* **2019**, *43*, 10878−10886.
(46) Bu, D.; Li, N.; Zhou, Y.; Feng, H.; Yu, F.; Cheng, C.; Li, M.; Xiao, L.; Ao, Y. Enhanced UV stability of N-halamine-immobilized Fe 3 O 4@ SiO 2@ TiO 2 nanoparticles: synthesis, characteristics and antibacterial property. *New J. Chem.* **2020**, *44*, 10352−10358.
(47) Muramatsu, H.; Kim, Y. A.; Yang, K. S.; Cruz-Silva, R.; Toda, I.; Yamada, T.; Terrones, M.; Endo, M.; Hayashi, T.; Saitoh, H. Rice husk-derived graphene with nano-sized domains and clean edges. *Small* **2014**, *10*, 2766−2770.
(48) Ge, H.; Ye, Z.; He, R. Raman spectroscopy of diesel and gasoline engine-out soot using different laser power. *J. Environ. Sci.* **2019**, *79*, 74−80.
(49) Kaur, A.; Chahal, P.; Hogan, T. Selective fabrication of SiC/Si diodes by excimer laser under ambient conditions. *IEEE Electron. Device Lett.* **2016**, *37*, 142−145.
(50) Yang, R.; Diao, Y.; Abayneh, B. Removal of Hg0 from simulated flue gas over silver-loaded rice husk gasification char. *R. Soc. Open Sci.* **2018**, *5*, No. 180248.
(51) Ghayeb Zamharir, S.; Karimzadeh, R.; Aboutalebi, S. H. Laser-assisted tunable optical nonlinearity in liquid-phase exfoliated MoS2 dispersion. *Appl. Phys. A* **2018**, *124*, No. 692.
(52) Mustapha, S.; Shuaib, D.; Ndamitso, M.; Etsuyankpa, M.; Sumaila, A.; Mohammed, U.; Nasirudeen, M. Adsorption isotherm, kinetic and thermodynamic studies for the removal of Pb (II), Cd (II), Zn (II) and Cu (II) ions from aqueous solutions using *Albizia lebbeck* pods. *Appl. Water Sci.* **2019**, *9*, No. 142.
(53) Gorzin, F.; Bahri Rasht Abadi, M. Adsorption of Cr (VI) from aqueous solution by adsorbent prepared from paper mill sludge: Kinetics and thermodynamics studies. *Adsorpt. Sci. Technol.* **2018**, *36*, 149−169.
(54) Lou, J. C.; Lee, R.; Chen, W.; Chang, C.; Hsu, K.; Han, J. Adsorption kinetics and thermodynamics of perchlorate on carbon nanotubes in water. *J. Environ. Eng.* **2014**, *140*, No. 04014038.
(55) Cardoso, N. F.; Lima, E. C.; Royer, B.; Bach, M. V.; Dotto, G. L.; Pinto, L. A.; Calvete, T. Comparison of *Spirulina platensis* microalgae and commercial activated carbon as adsorbents for the removal of Reactive Red 120 dye from aqueous effluents. *J. Hazard. Mater.* **2012**, *241*−*242*, 146−153.
(56) Nadafi, K.; Vosoughi, M.; Asadi, A.; Borna, M. O.; Shirmardi, M. Reactive Red 120 dye removal from aqueous solution by adsorption on nano-alumina. *J. Water Chem. Technol.* **2014**, *36*, 125−133.
(57) Muangrak, W.; Thouchprasitchai, N.; Phongboonchoo, Y.; Pongstabodee, S. Dual Functional Composite of Montmorillonite-Rich/Chitosan (MCC) for Decolorizing the Water Used in Joss Paper Process: Thermodynamic, Isotherm, and Kinetic Studies. *Appl. Sci.* **2020**, *10*, No. 7493.
(58) Wang, J.; Guo, X. Adsorption kinetic models: Physical meanings, applications, and solving methods. *J. Hazard. Mater.* **2020**, *390*, No. 122156.
(59) Kaveeshwar, A. R.; Kumar, P. S.; Revellame, E. D.; Gang, D. D.; Zappi, M. E.; Subramaniam, R. Adsorption properties and mechanism of barium (II) and strontium (II) removal from fracking wastewater using pecan shell based activated carbon. *J. Cleaner Prod.* **2018**, *193*, 1−13.
(60) Jagadeesh, R. V.; Murugesan, K.; Alshammari, A. S.; Neumann, H.; Pohl, M.-M.; Radnik, J.; Beller, M. MOF-derived cobalt nanoparticles catalyze a general synthesis of amines. *Science* **2017**, *358*, 326−332.
(61) Gürses, A.; Hassani, A.; Kıranşan, M.; Açışlı, Ö.; Karaca, S. Removal of methylene blue from aqueous solution using by untreated lignite as potential low-cost adsorbent: kinetic, thermodynamic and equilibrium approach. *J. Water Process Eng.* **2014**, *2*, 10−21.
(62) Karaca, S.; Gürses, A.; Açışlı, Ö.; Hassani, A.; Kıranşan, M.; Yıkılmaz, K. Modeling of adsorption isotherms and kinetics of Remazol Red RB adsorption from aqueous solution by modified clay. *Desalin. Water Treat.* **2013**, *51*, 2726−2739.
(63) Cardoso, N. F.; Lima, E. C.; Royer, B.; Bach, M. V.; Dotto, G. L.; Pinto, L. A.; Calvete, T. Comparison of *Spirulina platensis* microalgae and commercial activated carbon as adsorbents for the removal of Reactive Red 120 dye from aqueous effluents. *J. Hazard. Mater.* **2012**, *241*−*242*, 146−153.
(64) Nadafi, K.; Vosoughi, M.; Asadi, A.; Borna, M. O.; Shirmardi, M. Reactive Red 120 dye removal from aqueous solution by adsorption on nano-alumina. *J. Water Chem. Technol.* **2014**, *36*, 125−133.
(65) Çelekli, A.; İlgün, G.; Bozkurt, H. Sorption equilibrium, kinetic, thermodynamic, and desorption studies of Reactive Red 120 on *Chara contraria*. *Chem. Eng. J.* **2012**, *191*, 228−235.
(66) Kittinaovarat, S.; Kansomwan, P.; Jiratumnukul, N. Chitosan/modified montmorillonite beads and adsorption Reactive Red 120. *Appl. Clay Sci.* **2010**, *48*, 87−91.
(67) Tabak, A.; Baltas, N.; Afsin, B.; Emirik, M.; Caglar, B.; Eren, E. Adsorption of Reactive Red 120 from aqueous solutions by cetylpyridinium-bentonite. *J. Chem. Technol. Biotechnol.* **2010**, *85*, 1199−1207.
(68) Sarma, P.; Kumar, R.; Pakshirajan, K. Batch and Continuous Removal of Copper and Lead from Aqueous Solution using Cheaply Available Agricultural Waste Materials. *Int. J. Environ. Res.* **2015**, *9* (2), 635−648. https://ijer.ut.ac.ir/article_938.html.
(69) Krishnasamy, S.; Sai Atchyuth, B. A.; Ravindiran, G.; Chidambaram, J.; Ramalingam, M.; Subramanian, R.; Dhaleelur Rahman, Z. R.; Razack, N. A. Decolourization of Reactive Red 120 Using Agro Waste-Derived Biochar. *Adv. Mater. Sci. Eng.* **2022**, *2022*, No. 2689385.
(70) Mashkoor, F.; Nasar, A. Magnetized *Tectona grandis* sawdust as a novel adsorbent: preparation, characterization, and utilization for the removal of methylene blue from aqueous solution. *Cellulose* **2020**, *27*, 2613−2635.
(71) Wang, Y.; Zhang, Y.; Li, S.; Zhong, W.; Wei, W. Enhanced methylene blue adsorption onto activated reed-derived biochar by tannic acid. *J. Mol. Liq.* **2018**, *268*, 658−666.
(72) Hamad, H. N.; Idrus, S. Recent Developments in the Application of Bio-Waste-Derived Adsorbents for the Removal of Methylene Blue from Wastewater: A Review. *Polymers* **2022**, *14*, No. 783.

https://doi.org/10.1021/acsomega.2c07034
ACS Omega 2023, 8, 9904−9918